Article

Positive Magnetoresistance and Chiral Anomaly in Exfoliated Type-II Weyl Semimetal T_d-WTe$_2$

Rajdeep Adhikari [1,*,†] , Soma Adhikari [1,†], Bogdan Faina [1], Marc Terschanski [2], Sophie Bork [2], Claudia Leimhofer [3] , Mirko Cinchetti [2] and Alberta Bonanni [1,*]

1   Institut für Halbleiter-und-Festkörperphysik, Johannes Kepler University, Altenbergerstr. 69,
     A-4040 Linz, Austria; soma.adhikari@jku.at (S.A.); Bogdan.Faina@jku.at (B.F.)
2   Department of Physics, TU Dortmund, Otto-Hahn-Straße 4, 44227 Dortmund, Germany;
     marc.terschanski@tu-dortmund.de (M.T.); sophie.bork@tu-dortmund.de (S.B.);
     mirko.cinchetti@tu-dortmund.de (M.C.)
3   Institut für Polymerwissenschaften, Johannes Kepler University, Altenbergerstr. 69, A-4040 Linz, Austria;
     claudia.leimhofer_1@jku.at
*   Correspondence: Rajdeep.Adhikari@jku.at (R.A.); Alberta.Bonanni@jku.at (A.B.);
     Tel.: +43-732-2468-9664 (A.B.)
†   These authors contributed equally to this work.

Abstract: Layered van der Waals semimetallic T_d-WTe$_2$, exhibiting intriguing properties which include non-saturating extreme positive magnetoresistance (MR) and tunable chiral anomaly, has emerged as a model topological type-II Weyl semimetal system. Here, $\sim$45 nm thick mechanically exfoliated flakes of T_d-WTe$_2$ are studied via atomic force microscopy, Raman spectroscopy, low-T/high-$\mu_0 H$ magnetotransport measurements and optical reflectivity. The contribution of anisotropy of the Fermi liquid state to the origin of the large positive transverse MR$_\perp$ and the signature of chiral anomaly of the type-II Weyl Fermions are reported. The samples are found to be stable in air and no oxidation or degradation of the electronic properties is observed. A transverse MR$_\perp$ $\sim$1200 % and an average carrier mobility of 5000 cm^{2}V^{-1}s^{-1} at $T = 5$ K for an applied perpendicular field $\mu_0 H_\perp = 7$ T are established. The system follows a Fermi liquid model for $T \leq 50$ K and the anisotropy of the Fermi surface is concluded to be at the origin of the observed positive MR. Optical reflectivity measurements confirm the anisotropy of the electronic behaviour. The relative orientation of the crystal axes and of the applied electric and magnetic fields is proven to determine the observed chiral anomaly in the in-plane magnetotransport. The observed chiral anomaly in the WTe$_2$ flakes is found to persist up to $T = 120$ K, a temperature at least four times higher than the ones reported to date.

Keywords: Weyl semimetals; mechanical exfoliation; topological semimetals; positive magnetoresistance; chiral anomaly

1. Introduction

The presence of accidental two-fold degeneracies in the electronic band structures of solids leads to linear energy dispersions in the vicinity of the energy-degenerate points or nodes [1–3]. The emerging low energy excitations near these degenerate points follow a photon-like linear dispersion and can be described by the Weyl equation [2,4]. The signatures of such low energy Weyl Fermion-like excitations in condensed matter systems were recently observed in bulk NbAs [5] and TaAs crystals [6,7]. These materials are symmetry-protected topological states of matter and are characterized by conduction and valence bands which join with a linear dispersion around a pair of Weyl nodes [2,3,5,6,8,9]. Like in high energy physics, in low energy condensed matter systems, the Dirac, Weyl and Majorana Fermions constitute the family of elementary Fermions [4,10,11] and are an appealing workbenck for future quantum technologies. The Weyl semimetals (WSM) are topological semimetals hosting Weyl quasiparticles (WQP) [2,3,12]. The WQPs are

massless spin-1/2 Fermions, but their dispersion resembles the one of photons, due to the effective relativistic symmetry and the gapless Weyl nodes. The momenta k of the WQPs are projected either parallel or antiparallel to their spins and are distinguished through the quantum number chirality χ. The quantum expectation value of the chiral current in WSM is not conserved [2,9,12], leading to non-conservation of the chiral current, also known as chiral anomaly or Adler–Bell–Jakiw (ABJ) anomaly [13–17]. In condensed matter physics, the WSM are either of type-I (WSM-I) or of type-II (WSM-II). The WSM-II are known to break the Lorentz symmetry, which is-in contrast- conserved in the type-I WSMs [2]. The violation of the Lorentz symmetry leads to a tilted Weyl cone in the momentum space and makes these materials compelling for the study of exotic Lorentz violation theories that are beyond the Standard Model [3]. The tilted Weyl cone combined with the broken chiral symmetry results in the onset of quantum mechanical and topological mechanisms, such as intrinsic anomalous Hall effects [18], Klein tunneling [19], Landau level collapse [20] and ABJ anomaly [13,16,17], both in WSM-I and in WSM-II.

The presence of tilted Weyl cones and of low energy excitations violating the Lorentz invariance in the vicinity of the Weyl points were predicted for the electronic band structure of WTe_2, a transition metal dichalcogenide (TMDC) semimetal with layered van der Waals structure [21,22]. In addition to the presence of the Fermi arc at the Fermi surface [23–25], anisotropic transport properties including extreme transverse magnetoresistance and the anisotropic ABJ anomaly, are reported for both bulk and few layers WTe_2 flakes [15,26–36]. The tilted Weyl cone was also observed in the TMDC semimetal $MoTe_2$ [37,38] and in LaAlGe [39]. Another characteristic feature of WTe_2 is the extreme positive transverse magnetoresistance $MR_\perp$, which can reach values as high as $10^5\%$ for magnetic fields ~ 9 T applied parallel to the $c-$axis of bulk or thin flakes of WTe_2 in the Fermi liquid phase at $T \sim 100$ mK [40–42]. In addition, evidence of topologically protected conducting edge states [43] and flat-band superconductivity in close proximity to Pd [44] and Nb [45] was shown in bulk and few layers WTe_2 flakes, while quantum spin Hall states are found in mechanically exfoliated monolayer WTe_2[46]. Most of the reported literature on T_d-WTe_2 concerns bulk crystals or mechanically exfoliated flakes. While the bulk crystals are chemically stable [40], the ultrathin exfoliated flakes of T_d-WTe_2 are reported to be prone to oxidation and require inert ambient for fabrication and sample processing [43]. In particular, it is not evident whether the crystal exfoliates along a preferred direction corresponding to the $a-$ or $b-$axes [14]. In addition, apart from the observed extreme positive $MR_\perp$, weak-antilocalization (WAL) and negative longitudinal magnetoresistance $MR_\parallel$ with chiral anomaly are reported in exfoliated flakes of T_d-WTe_2 [14,34].

Here, mechanically exfoliated ~ 45 nm thin flakes of T_d-WTe_2 are studied via atomic force microscopy (AFM), Raman spectroscopy, optical reflectivity and low-T/high-$\mu_0 H$ magnetotransport measurements. Beside confirming the chemical stability of the system in ambient conditions, a Fermi liquid behavior is found, with large positive $MR_\perp$ up to $\sim 1200\%$, average carrier mobility $\mu_{av} \sim 5000$ cm^{2}V^{-1}s^{-1} and chiral anomaly persisting up to $T \sim 120$ K.

2. Materials and Methods

The WTe_2 flakes are fabricated via mechanical exfoliation from a bulk (mother) crystal obtained commercially from hqgraphene (http://www.hqgraphene.com (accessed on 1 September 2019). Micromechanical cleavage is repeated using fresh Nitto tapes until ~ 45 nm thin flakes are obtained. Upon exfoliation, the flakes are transferred onto Gelpack Grade 4 viscoelastic polydimethylsiloxane (PDMS) stamps with a rigid metallic support. The mechanical exfoliation process results in an ensemble of flakes with diverse sizes, geometries and thicknesses, distributed over the PDMS stamp. The exfoliated flakes on the PDMS are then analysed for thickness and number of layers using a high resolution Keyence VHX-7000 optical microscope (Keyence, Osaka, Japan) operated in transmission mode. Flakes of uniform thickness are then transferred onto prepatterned SiO_2/p^{++}-Si substrates with markers and metal contact pads. The flakes transferred onto the pristine substrates

are used for AFM, Raman spectroscopy and optical measurements, while the samples fabricated on the prepatterned substrates are employed to study the electronic properties of the exfoliated WTe$_2$ flakes by low-T/high-$\mu_0 H$ magnetotransport measurements.

The (1×1) cm^2 SiO$_2$/p^{++}-Si substrates with a SiO$_2$ thickness of 90 nm are spin coated with S1805 positive photoresist followed by soft baking at 90 °C. A Süss Mask aligner photolithography system is employed to expose the S1805 coated substrates to an ultraviolet mercury lamp through a window mask. The substrates are developed using a conventional MS-519 photolithography developer and subsequently transferred into a sputtering chamber for the deposition of 10 nm thick Pt contacts. The metallic contact pads in van der Pauw 4-probe geometry are then obtained by rinsing away the photoresist with warm acetone for 15 seconds in an ultrasonic bath.

The exfoliated WTe$_2$ flakes are transferred onto both pristine and prepatterned substrates using an indigeneously developed viscoelastic dry transfer system [47]. Gold wires with a diameter of 25 μm are bonded to the Pt contact pads using In as conducting adhesive. It is worth noting, that the mechanical exfoliation and the viscoelastic dry transfer are carried out in air ambient. The stability of the samples in ambient conditions is discussed in the next section. This is in contrast to what generally reported in literature, where the fabrication and transfer of the flakes takes place in vacuum or in inert atmosphere [28,43]. The entire procedure of sample fabrication and including the mechanical exfoliation, the viscoelastic dry transfer of the WTe$_2$ flakes on prepatterned Pt contacts, the Au wire bonding and the transfer of the samples into the cryostat for measurements is achieved in less than 30 min, thereby ensuring minimal oxidation of the flakes. This fabrication protocol minimizes the detrimental effects of surface oxidation on the electronic properties of the WSM-II WTe$_2$ [48,49].

A schematic representation of the semimetallic bulk crystal structure of T_d-WTe$_2$ highlighting the $a-$, $b-$ and $c-$ directions of the space group C_{2v}^7 ($Pmn2_1$) distorted orthorhombic basis, is shown in Figure 1a. Each unit cell is composed of two W and four Te atoms and the W-Te bond lengths vary between 2.7 Å and 2.8 Å [40,50]. The bulk WTe$_2$ exhibits a T_d stacking order in which the atoms in the upper layer are rotated by 180 ° w.r.t. the atoms in the lower layer, as sketched in Figure 1a. In the T_d-WTe$_2$, the a-axis is populated by the W-chain while the axis b is orthogonal to it. The $c-$axis is perpendicular to the $ab-$ plane. Two exemplary samples are considered, namely:
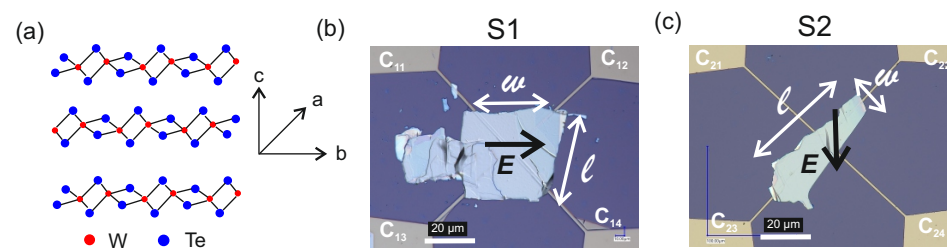

Figure 1. (**a**): Schematic illustration of the crystal structure of T_d-WTe$_2$ showing the directions of the $a-$, $b-$, and $c-$axes. (**b**,**c**): Optical image of the WTe$_2$ samples S1 and S2, respectively.

(i) Sample S1: in the van der Pauw geometry the excitation current I_{ac} is applied between the contacts C$_{11}$ and C$_{12}$ while the resulting voltage V_{xx} is measured across C$_{13}$ and C$_{14}$, so that the electric field E due to I_{ac} is aligned exactly along w, as visualized in the optical microscopy image in Figure 1b;

(ii) Sample S2: in the van der Pauw geometry I_{ac} is applied between the contacts C$_{21}$ and C$_{22}$ while V_{xx} is measured across C$_{23}$ and C$_{24}$, so that E is slightly misaligned with respect to w, as evidenced in the optical microscopy image in Figure 1c.

The length and width of the rectangle-like flakes are indicated by l and w, respectively. In the absence of a conclusive evidence for the precise orientations of the $a-$ and $b-$axes, the geometry of the studied flakes is described by l and w, while the $c-$axis is the one perpendicular to the plane of the flakes.

3. Results and Discussions

3.1. Atomic Force Microscopy and Raman Spectroscopy

The surface morphology and the thickness of the WTe$_2$ flakes are measured using a VEECO Dimension 3100 AFM system. The AFM image of a WTe$_2$ flake transferred onto a SiO$_2$/p^{++}-Si substrate is provided in Figure 2a. The height profile of the flake is analysed using the Gwiddyon data analysis software and a thickness of 45 nm is determined. The surface morphology of the flake is shown in Figure 2b and a root mean square surface roughness of ∼0.45 nm is estimated.
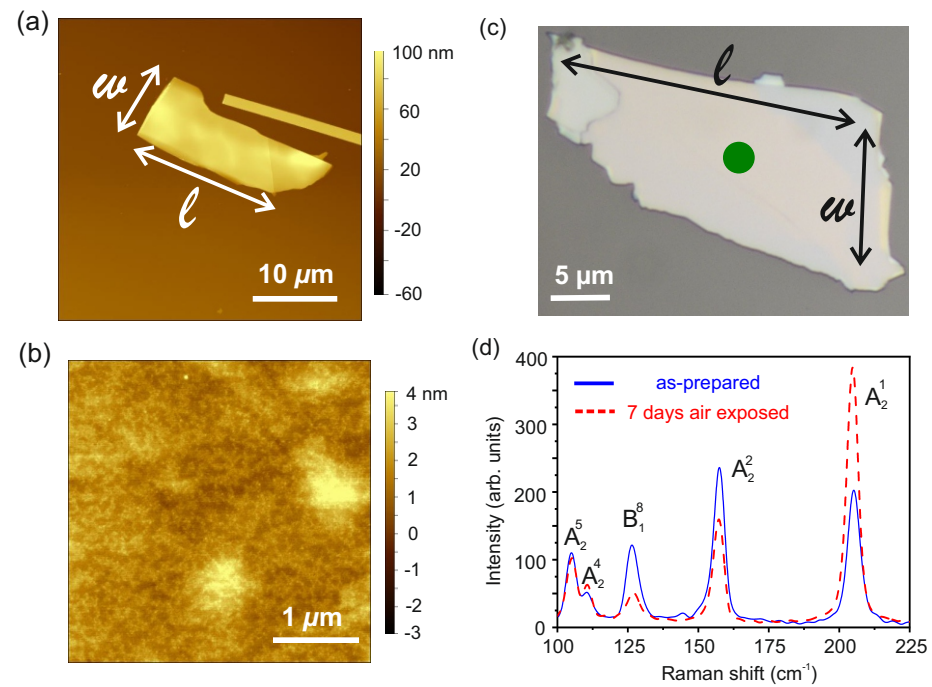

Figure 2. (**a**): AFM image of an exfoliated WTe$_2$ flake dry transferred onto the SiO$_2$/p^{++}-Si substrate. (**b**): Surface morphology recorded for a (3.5×3.5) μm^2 AFM scan area of the transferred WTe$_2$ flake. (**c**): Optical microscopic image of 45 nm thick WTe$_2$ flake used to measure Raman spectroscopy. The dot indicates the position of the laser spot during the Raman measurements. (**d**): Raman spectra collected from the specimen in (**c**) as-prepared and after seven days of exposure to air ambient.

The chemical stability and crystallographic phase of the WTe$_2$ flakes are studied using Raman spectroscopy carried out in a WIRec Alpha 300 R-Raman-System with a double frequency Nd:YAG laser of wavelength 532 nm. The objective allows a laser beam spot diameter of ∼2 μm. The samples are positioned on a XY-translation stage and a camera system enables guiding the sample in the laser spot. A total of 33 Raman vibrations are predicted by group theory [51] and the irreducible representation of the optical phonons at the Γ point of the Brilloiun zone of the bulk T_d−WTe$_2$ is given by:

$$\Gamma_{\text{bulk}} = 11A_1 + 6A_2 + 11B_1 + 5B_2 \tag{1}$$

where A_1, A_2, B_1 and B_2 are Raman active phonon modes. In this work, the Raman modes have been excited along the c−axis of the T_d−WTe$_2$ crystal, i.e., the laser beam is directed perpendicular to the plane of the WTe$_2$ flake and of the substrate. Since the Raman excitations reported here are unpolarized, neither the incident, nor the scattered electric field vectors $\vec{e}_\mathrm{i}$ and $\vec{e}_\mathrm{s}$ are aligned along the a− or c−axes. An optical microscopy image of the flake studied by Raman spectroscopy is shown in Figure 2c, while the room temperature Raman spectra recorded for the as-prepared and air aged WTe$_2$ flake are given in Figure 2d. A total of five Raman active modes with peaks centered at 105.0 cm^{-1}, 110.5 cm^{-1}, 126.5 cm^{-1}, 157.2 cm^{-1}, and 205.3 cm^{-1} have been recorded. The Raman active

modes are labelled as A_q^p and B_q^p, where q $= \{1, 2\}$ and p $\in \mathbb{Z}$ to uniquely identify the Raman mode. Here, the five detected Raman peaks are assigned to the A_2^5, A_2^4, B_1^8, A_2^2, and A_2^1 allowed Raman active modes [50,51]. Upon comparison with the calculated resonances, it is found that the experimental A_2^4 is blue shifted, while the other four Raman active modes are red shifted due to the stress built up when the flake is transferred onto the rigid substrate. Upon measurement, the sample has been exposed to air for seven days and then Raman spectra have been recorded. The Raman spectrum for the air aged sample, represented by the dashed curve in Figure 2d is found to show the allowed Raman modes of the optical phonons as recorded for the pristine flake. No peaks related to oxides of Te or W are detected, confirming the chemical stability of the WTe_2 flakes.

3.2. Out-of-Plane Magnetotransport

Low-T/high-$\mu_0 H$ magnetotransport measurements are carried out on the samples S1 and S2 in a Janis Super Variable Temperature 7TM-SVM cryostat (Janis Cryogenics, Westerville, OH, USA) equipped with a 7 T superconducting magnet. Prior to the measurements, the Ohmic nature of the Pt contacts to the WTe_2 flakes is confirmed by the linear $I - V$ characteristics measured with a high precision Keithley 4200 SCS dc source-measure unit (SMU). The longitudinal resistance R_{xx} as a function of T and $\mu_0 H$ has been measured by employing a lock-in amplifier (LIA) ac technique. The I_{ac} is sourced from a Standord Research SR830 LIA, while the generated voltage V_{xx} is measured in a phase locked mode as a function of T and $\mu_0 H$. The applied current is limited to 10 μA to minimize Joule heating and subsequent thermogalvanic effects due to the constraints imposed by the low dimensionality of the samples. The lock-in expand function is employed to enhance the sensitivity of the LIA. All measurements have been performed at a frequency of 127 Hz. The chosen reference axes for the applied $\mu_0 H$, for E due to I_{ac}, and for the l and w dimensions of the specimens - identified to characterize the transverse magnetoresistance $MR_\perp$ and the longitudinal magnetoresistance $MR_\parallel$-are shown in Figure 3a,b, respectively. In Figure 3a, θ is the angle between $\mu_0 H_\perp$ applied along the $c-$axis and the $ab-$plane, while E is oriented along w. The $\mu_0 H_\perp$ has been recorded for $\theta = 0°$ and $90°$. The $MR_\parallel$ for S1 and S2 are measured by applying an in-plane magnetic field $\mu_0 H_\parallel$ at an angle ψ w.r.t. E, while E is always applied along w. Thus, there are two possible configurations of the relative orientations of E, $\mu_0 H_\parallel$ w.r.t. w, namely: (i) $\left[\mu_0 H_\parallel \parallel (E \parallel w) \right]$ and (ii) $\left[\mu_0 H_\parallel \perp (E \parallel w) \right]$.

The evolution of longitudinal resistance R_{xx} as a function of T in the interval $5\,K \leq T \leq 225\,K$ for S1 and for S2 is given in Figure 4a,b, respectively. The R_{xx}–T behavior is studied while the samples are cooled down, both for $\mu_0 H_\perp = 0$ and for $\mu_0 H_\perp \neq 0$ and the measurements are referred to as zero field cooled (ZFC) and field cooled (FC), respectively. The FC R_{xx} are measured by applying $\mu_0 H_\perp = 3$ T and 7 T, as shown in Figure 4a,b. The monotonous decrease of R_{xx} with decreasing T for $\mu_0 H_\perp = 0$ is a signature of the metallic behavior of the exfoliated T_d-WTe_2 flakes. For $\mu_0 H_\perp \geq 3\,T$, R_{xx} essentially follows the ZFC behavior down to T_{Trans}. At $T = T_{Trans}$—indicated by the arrows (↓) in Figure 4a,b—a transition in the electronic phase of the flakes from metallic to insulating is found for both S1 and S2. This behavior is consistent with the one previously observed for bulk and thin T_d-WTe_2 layers [35,40,42,52,53]. It is also noted, that the magnitude of the $\mu_0 H_\perp$- induced change in R_{xx} increases with decreasing T and with increasing $\mu_0 H_\perp$. The magnetoresistance, defined as:

$$\text{MR} = \frac{R_{xx}(\mu_0 H) - R_{xx}(0)}{R_{xx}(0)} \times 100\% \qquad (2)$$

is a fingerprint of the microscopic physical mechanism governing the electronic properties of any trivial or non-trivial electronic system. Here, $R_{xx}(\mu_0 H)$ and $R_{xx}(0)$ are the resistances of the system under an applied field $\mu_0 H$ and in zero field, respectively. The $MR_\perp$ of the two samples S1 and S2 are estimated as a function of an applied field $\mu_0 H_\perp$ at different T in the range $5\,K \leq T \leq 150\,K$ and are reported in Figure 4c,d. Large positive $MR_\perp \sim 1200\%$

and $\sim$800% are found at $T = 5$ K, under the maximum applied field $\mu_0 H_\perp = 7$ T for S1 and S2, respectively. The estimated $MR_\perp$ for both samples follow the power-law behavior $MR \sim mH^n$ [42,54], where m is a proportionality constant and $n \in \mathbb{R}$ is the power index. The value of n is estimated by numerical fitting of the $MR_\perp$ behavior for both S1 and S2 as a function of $\mu_0 H_\perp$ and is found to be $1.9 \leq n \leq 2.1$ in the range 5 K $\leq T \leq 150$ K [35,40–42]. It is noted, that no Shubnikov-de Haas (SdH) oscillations have been observed in the $MR_\perp$ of both samples, even up to the maximum $\mu_0 H_\perp$. The $MR_\perp$ as a function of $\mu_0 H_\perp$ for $\theta = 0°$ and $90°$ and $T = 5$ K are also recorded for S1 and S2 and reported in Figure 4e,f, respectively. An anisotropic behavior of $MR_\perp$ is observed for the T_d-WTe$_2$ flakes studied here [7,15,42,53].
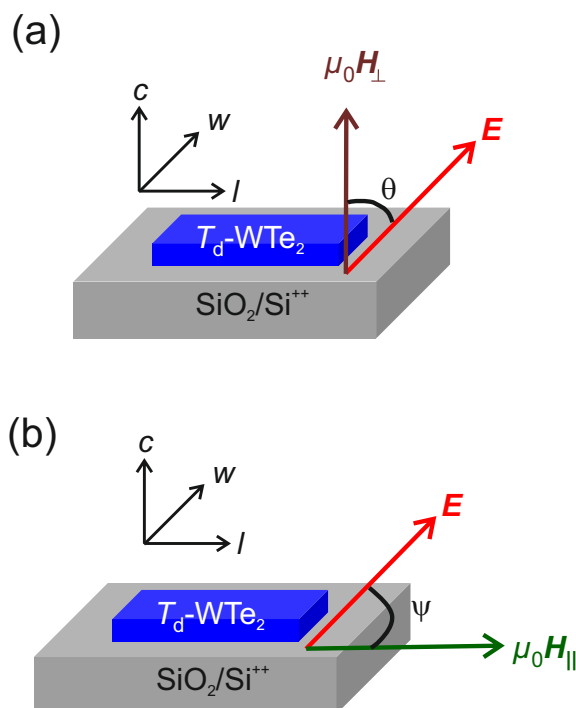

Figure 3. Schematic illustration of the relative orientations of E, $\mu_0 H$, l and w relevant for the measurements of (**a**): $MR_\perp$ and (**b**): $MR_\parallel$.

The evolution of $MR_\perp$ as a function of T for $\mu_0 H_\perp = 3$ T and $\mu_0 H_\perp = 7$ T is shown in Figure 5a,b for S1 and S2, respectively. The positive $MR_\perp$ sets in for $T \leq 75$ K and for a critical field $\mu_0 H_c \geq 3$ T, in accord with the R_{xx}-T behavior previously discussed. A relevant feature of the observed large $MR_\perp$, is the presence of a magnetic field-dependent critical turn-on temperature T_{Trans} for $\mu_0 H_\perp \geq 3$ T. However, such critical temperature is absent when the samples are cooled down in the presence of the field $\mu_0 H_\parallel$. The transition from metallic to insulating state is observed in several other material systems exhibiting colossal positive MR, where the extreme magnitude of the MR is attributed to a magnetic field-driven metal-to-insulator (MIT) transition [55–57], due to a field-induced excitonic gap in the linear spectrum of the Coulomb interacting quasiparticles, leading to an excitonic insulator phase [42,58]. The excitonic gap is expected to follow the relation: $\Delta_T(\mu_0 H - \mu_0 H_c) \rightarrow [\mu_0 H - \mu_0 H_c(T)]^{\frac{1}{2}}$, where $\mu_0 H_c$ is the threshold magnetic field and the dependence of the excitonic gap on the magnetic field is characteristic of a second order phase transition.
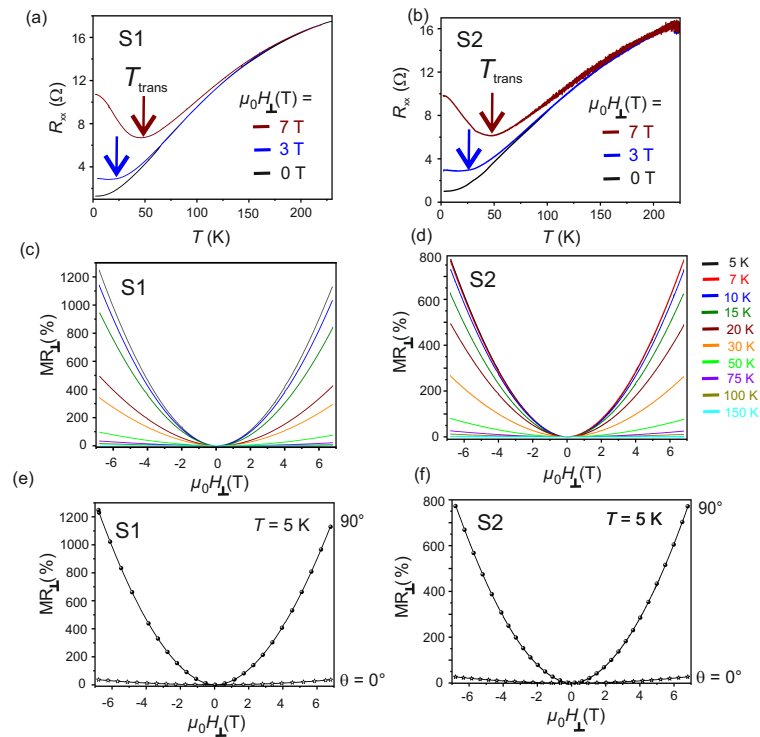
Figure 4. (**a,b**): R_{xx} as a function of T at $\mu_0 H_\perp = 0\,\mathrm{T}$, $\mu_0 H_\perp = 3\,\mathrm{T}$ and $\mu_0 H_\perp = 7\,\mathrm{T}$ for S1 and S2, respectively. (**c,d**): $\mathrm{MR}_\perp$ as a function of $\mu_0 H_\perp$ measured in the range $5\,\mathrm{K} \leq T \leq 150\,\mathrm{K}$ for S1 and S2, respectively. (**e,f**): $\mathrm{MR}_\perp$ as a function of $\mu_0 H$ at $\theta = 0°$ and $\theta = 90°$ at $T = 5\,\mathrm{K}$ for S1 and S2, respectively.
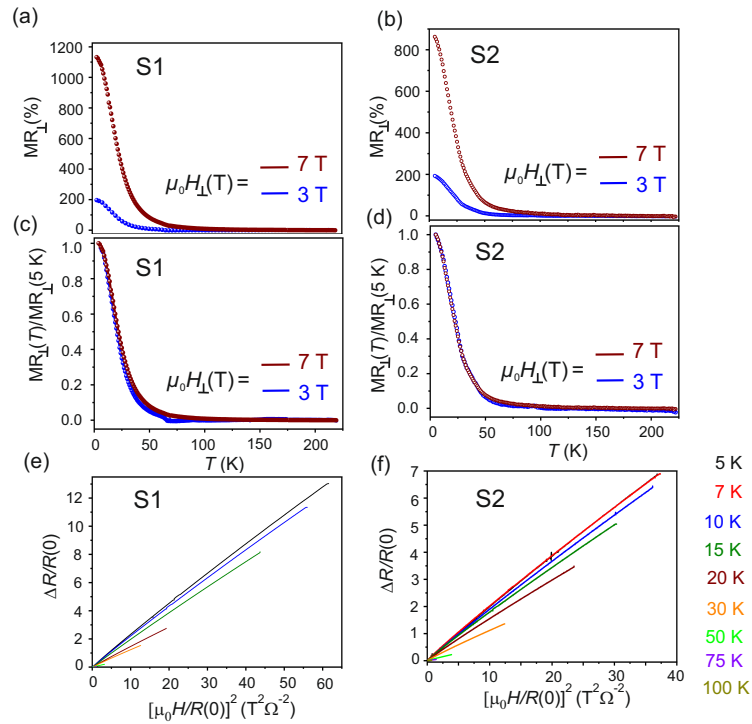
Figure 5. (**a,b**): FC transverse MR as a function of T recorded for $\mu_0 H_\perp = 3\,\mathrm{T}$ and $7\,\mathrm{T}$ for samples S1 and S2, respectively. (**c,d**): Estimated normalized $\mathrm{MR}_\perp$ defined as the ratio of $\mathrm{MR}_\perp(T)$ to $\mathrm{MR}_\perp(5\,\mathrm{K})$ recorded by applying $\mu_0 H_\perp = 3\,\mathrm{T}$ and $\mu_0 H_\perp = 7\,\mathrm{T}$ for S1 and S2, respectively. (**e,f**): calculated Kohler's plots of S1 and S2 in the range $5\,\mathrm{K} \leq T \leq 100\,\mathrm{K}$.

The normalized $MR_\perp$ for S1 and S2, defined as the ratio between $MR_\perp$ measured at any T ($MR_\perp(T)$) and $MR_\perp$ at $T = 5$ K ($MR_\perp(5K)$), are plotted as a function of T for $\mu_0 H_\perp = 3$ T and $\mu_0 H_\perp = 7$ T in Figure 5c,d, respectively. It is observed, that the $MR_\perp$ have the same T-dependence for both S1 and S2 WTe_2 flakes, as inferred from the collapse of the two curves. This behavior of the normalized $MR_\perp$ is inconsistent with the existence of a $\mu_0 H$-dependent excitonic gap [42,53,58]. It is, thus, concluded that the origin of the MIT observed here in the R_{xx}–T behavior for $\mu_0 H_\perp \geq 3$ T, lies in the evolution of the electronic structure of T_d-WTe_2. From angle-dependent photoemission spectroscopic studies on bulk T_d-WTe_2, it was shown that the presence of minute electron and hole pockets of equal size at low T is responsible for the remarkably large positive $MR_\perp$, due to a T-dependent charge compensation mechanism [25,59]. The anisotropic behaviour of the Fermi surface of T_d-WTe_2 is reflected in an anisotropic $MR_\perp$ as a function of the direction of $\mu_0 H$ defined by θ, which is also observed in the T_d-WTe_2 flakes measured in this work, as evidenced in Figure 5e,f. Similar results are obtained when a 45 nm thick T_d-WTe_2 flake is contacted with Au (instead of Pt) and the results are shown in Figures S4 and S5 of the Supplementary Materials. Therefore, it can be concluded, that the transverse magnetotransport properties of mechanically exfoliated T_d-WTe_2 are independent of the metal employed to contact the semimetallic flakes and also of the exposure of the flakes to air ambient.

The presence of the electron and hole pockets in the elctronic bands of T_d-WTe_2 is probed by a Kohler's analysis of the R_{xx}–$\mu_0 H_\perp$ curves at different T. According to the Kohler's theory, the change in the isothermal longitudinal resistance R_{xx} for a conventional metal in an applied field $\mu_0 H$ obeys the functional relation:

$$\frac{\Delta R_{xx}}{R(0)} = F\left(\frac{\mu_0 H}{R(0)}\right) \tag{3}$$

where $R(0)$ is the ZFC resistance at T. The Kohler's behavior is due to the fact, that conventional metals host a single kind of charge carriers. In a weak field limit, the MR of most metals follows a quadratic dependence on $\mu_0 H$, i.e., $MR \propto (\alpha + \beta \mu_0 H^2)$, with α and β proportionality constants [54]. The resistance $R(0)$ is $\propto \frac{1}{\tau}$, where τ is the scattering time of the itinerant charge carriers in a metallic system. Therefore, a plot of $\frac{\Delta R_{xx}}{R(0)}$ vs. $\left(\frac{H}{R(0)}\right)^2$ is expected to collapse into a single T-independent curve, provided that the number of charge carriers, the type of charge carriers, and the electronic disorder in the system remain constant over the measured T range. The Kohler's plots for S1 and S2 measured at various T are reported in Figure 5e,f, respectively. A significant deviation is observed in the scaled transverse $MR_\perp$. Due to spin dependent scattering, such deviations are common in magnetically doped topological systems [60], but in a non-magnetic system such as T_d-WTe_2 this behavior indicates that the electronic bands contain both electrons and holes as charge carriers. Therefore, the formation of excitons leads to a change in the carrier density, resulting in the observed deviation from the Kohler's rule in the thin flakes of T_d-WTe_2 as observed previously in bulk systems [42,59]. However, as reported by Wang et al. [61], bulk T_d-WTe_2 crystal grown by chemical vapour transport follows the Kohler's rule, which is in contrast to the behavior observed here.

The values of the average carrier mobility μ_{av}, i.e., the mean value of the electron and hole mobilities, are calculated for both samples considered here, by fitting $MR_\perp$ with the Lorentz law [41,54] according to the relation:

$$\frac{\Delta R}{R(0)} = \left[1 + (\mu_{av}\mu_0 H)^2\right] \tag{4}$$

The estimated μ_{av} for S1 and S2 as a function of T are provided in Figure 6. Due to the dominant electron-phonon correlation, a monotonic decrease of μ_{av} is observed for $T > 50$ K, both in S1 and S2. However, for $T \leq 50$ K, the estimated values of μ_{av} with decreasing T exhibit a plateau in the logarithmic scale with estimated $\mu_{av} \simeq 5000$ cm^{2}V^{-1}s^{-1} and $\mu_{av} \simeq 4000$ cm^{2}V^{-1}s^{-1} at $T = 5$ K for S1 and S2, respectively. The values of μ_{av}

obtained in this work are higher than those reported in literature for ultra-thin $\sim$9 nm flakes [35] measured at $T = 5$ K, but are comparable to those reported for bulk crystals of T_d-WTe$_2$ grown with the Te-flux method [62]. The high carrier mobility in semimetallic T_d-WTe$_2$ at low T points at a deviation from the electron-phonon coupling-dominated carrier transport.
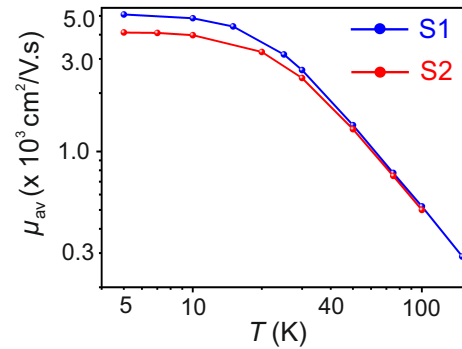

Figure 6. μ_{av} as a function of T for samples S1 and S2.

A deviation from linear behavior originating from the electron-phonon coupling at $T \geq 50$ K is observed in the zero-field cooled R_{xx} as a function of T for both S1 and S2, as previously reported in Figure 4a,b, respectively. The behavior of R_{xx} as a function of T in the range 5 K $\leq T \leq 50$ K is presented in Figure 7a,b for S1 and S2 and it follows the predictions of the Fermi liquid theory [42,54,59] with $R_{xx} = \gamma_0 + \gamma' T^2$, where γ_0 and γ' are proportionality constants. For 5 K $\leq T \leq 50$ K, electron-electron correlation is found to be the dominant mechanism in the Fermi liquid state of thin flakes of semimetallic T_d-WTe$_2$ [25,42,59]. Thus, it is concluded, that the observed large positive MR$_\perp$ occurs in the Fermi liquid state of the system, as endorsed by the observed anisotropic behavior of MR$_\perp$, which is a signature of an anisotropic Fermi surface [25,40–42,59].
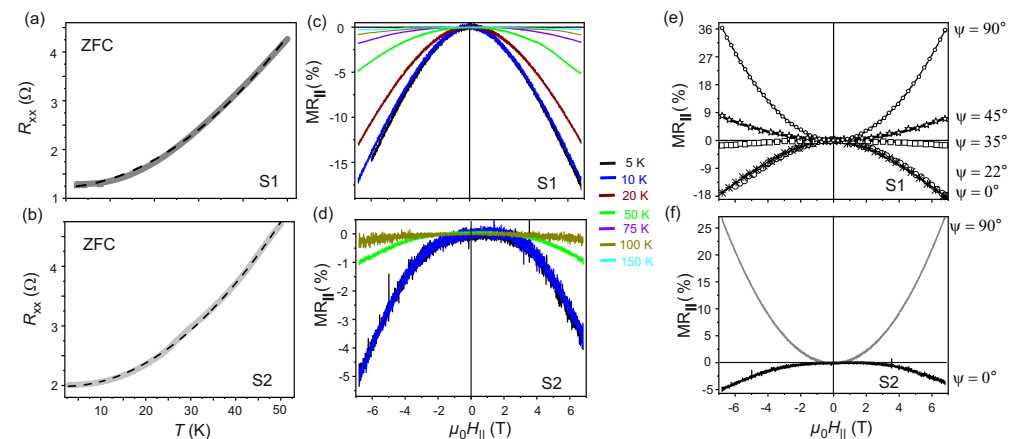

Figure 7. (**a**,**b**): R_{xx} as a function of T with $\mu_0 H_\perp = 0$ T for S1 and S2, respectively. (**c**,**d**): MR$_\parallel$ recorded as a function of $\mu_0 H_\parallel$ in the range 5 K $\leq T \leq 100$ K for S1 and S2, respectively. (**e**,**f**): MR$_\parallel$ as a function of the azimuthal angle ψ at $T = 5$ K for S1 and S2, respectively.

3.3. In-Plane Magnetotransport

The electronic band structure of WSM-II is characterized by the presence of an asymmetric electron dispersion responsible for the anisotropy in the electronic properties of these systems. In WSM-II, the breaking of the Lorentz invariance and of the chiral symmetry in massless Weyl Fermions under quantum fluctuations leads to the chiral anomaly, which is observed as a negative MR$_\parallel$ under the condition of $(\mu_0 H \parallel E)$. In particular, for the case of T_d-WTe$_2$, for $[\mu_0 H \parallel (E \parallel b)]$, the signature negative MR$_\parallel$, anisotropic in the *ab*-plane of the orthorhombic lattice, is observed [14,34,52]. In the mechanically exfoliated flakes studied

here, the directions of the $a-$ and the $b-$axes are not determined *a priori*. As discussed above, the orientation of the studied flakes is therefore defined in terms of the dimensions w and l. Here, E is always parallel to w, while $\mu_0 H_\parallel$ is applied at an azimuthal angle ψ w.r.t. $(E \parallel w)$. The angle ψ is varied between $0°$ and $90°$. The $MR_\parallel$ has been estimated for both S1 and S2. The recorded $MR_\parallel$ for S1 and S2 at $T = 5\,K$ are reported in Figure 7c,d, respectively. For S1, $MR_\parallel$ is recorded for $\psi = 0°$, $22°$, $35°$, $45°$ and $90°$. It is found, that the negative $MR_\parallel$ due to the chiral anomaly disappears for $\psi \gtrsim 35°$. For sample S2, $MR_\parallel$ is collected for $\psi = 0°$, and $90°$ solely to show the signature of anisotropy in $MR_\parallel$ and the chiral anomaly. Negative $MR_\parallel$ of magnitude -18% and -5% for $\mu_0 H_\parallel = 7\,T$ are observed at $T = 5\,K$ and $\psi = 0°$ for S1 and S2, respectively. The negative $MR_\parallel$ for $\left[\mu_0 H_\parallel \parallel (E \parallel w) \right]$ is a signature of chiral anomaly. The magnitude of $MR_\parallel$ decreases with increasing T and vanishes at $T \geq 150\,K$, as shown in Figure 7c,d for S1 and S2, respectively.

The magnitude of the negative $MR_\parallel$ is reduced on deviating from the parallel condition, i.e., for $\psi > 0°$. As depicted in Figure 7e, the magnitude of $MR_\parallel$ estimated at $\psi = 22°$ is comparable to the one assessed for $\psi = 0°$. However, for $\psi = 35°$, a $MR_\parallel \sim -1\%$ is determined, which then reverses sign for increasing ψ and a positive $MR_\parallel$ is measured for $\psi = 45°$ and $\psi = 90°$, respectively. Therefore, it is inferred that the assigned w axis of the flakes studied here is indeed aligned along the $b-$axis of the distorted rhombohedral unit cell of T_d-WTe$_2$. Further, it is also established that the topological pumping of the chiral charge current in the WSM-II T_d-WTe$_2$ occurs when $\mu_0 H_\parallel$ is applied at angles $\psi < 35°$ w.r.t. $E \parallel w$. For $\left[\mu_0 H_\parallel \perp (E \parallel w) \right]$, i.e., at $\psi = 90°$, a $MR_\parallel = +36\%$ for $\mu_0 H_\parallel = 7\,T$ at $T = 5\,K$ is found, as shown in Figure 7e. Similar behavior is also observed for sample S2, as reported in Figure 7f. However, the reduced magnitude of $MR_\parallel$ to -5% for $\psi = 0°$ indicates that for this flake, w is not aligned along the $b-$axis. The estimated values of $MR_\perp$, $MR_\parallel$, μ_{av} at $T = 5\,K$ and the critical T up to which the chiral anomaly persists for samples S1 and S2 are summarized in Table 1.

Table 1. Estimated values of $MR_\perp$, $MR_\parallel$ and μ_{av} at $T = 5\,K$ and the critical temperature for observation of chiral anomaly in samples S1 and S2.

	$MR_\perp$ (%); $T = 5\,K$; $\theta = 90°$	$MR_\parallel$ (%); $T = 5\,K$; $\psi = 90°$	$MR_\parallel$ (%); $T = 5\,K$; $\psi = 0°$	μ_{av} (cm^2/V.s); $T = 5\,K$	Critical T (K)
S1	1200	36	−18	5000	120
S2	800	27	−5	4100	80

To prove that $\left[\mu_0 H_\parallel \parallel (E \parallel w) \right]$ is the necessary and sufficient condition to observe chiral anomaly in WTe$_2$ and to confirm the reproducibility of the obtained results, a third sample S3 is fabricated following the methods described above and the $MR_\parallel$ is measured as a function of T. For S3 in the van der Pauw geometry, I_{ac} is applied between the contacts C_{31} and C_{32} while V_{xx} is measured across C_{33} and C_{34}, so that E is along w, as shown in the optical microscopy image given in Figure 8a. The value of $MR_\parallel$ measured for $\mu_0 H_\parallel = 7\,T$ as a function of T is reported in Figure 8b for S1, S2 and S3. The measured $MR_\parallel$ persists up to $T \simeq 120\,K$ for both S1 and S3, while for S2 the negative $MR_\parallel$ survives up to $T = 100\,K$. As seen in Figure 8b, the magnitude of $MR_\parallel$ and its dependence on T are identical for S1 and S3, while the magnitude of $MR_\parallel$ for S2 is reduced. This is due to the slight misalignment of the $w-$axis w.r.t. I_{ac} in S2. The critical T below which chiral anomaly can be observed in thin flakes of WTe$_2$ reported in this work is at least four times higher than the one reported by Li et al. [34] who observed chiral anomaly up to 30 K. In contrast to those reported in literature [34], the WTe$_2$ flakes used in this work are not exposed to any chemical or e-beam irradiation during the sample fabrication process. The pristine nature of the flakes used in this work is taken to be the reason for the observed critical temperature of 120 K. Additionally, the magnitude of $MR_\parallel \sim 18\%$ measured at $T = 5\,K$ and $\mu_0 H_\parallel = 7\,T$ for S3 is one order of magnitude higher than the one already reported [34,63].
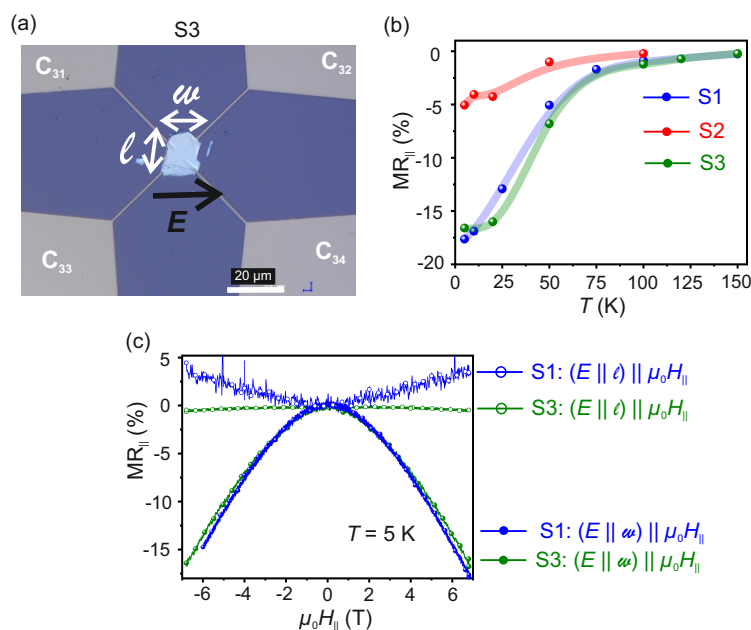
Figure 8. (**a**): Optical image of the sample S3. (**b**): Negative $MR_\parallel$ as a function of $\mu_0 H_\parallel$ — a fingerprint of the chiral anomaly measured for the configuration $\left[\mu_0 H_\parallel \parallel (E \parallel w)\right]$ for samples S1, S2 and S3. (**c**): $MR_\parallel$ measured at $T = 5\,\text{K}$ for samples S1 and S3 in the configurations $\left[\mu_0 H_\parallel \parallel (E \parallel l)\right]$ and $\left[\mu_0 H_\parallel \parallel (E \parallel w)\right]$.

The observations of negative $MR_\parallel$ or negative longitudinal magnetoresistance (NLMR) in bulk crystals of topological semimetals were shown to be dominated by current jetting [64–69]. Similar NLMR are found in bulk crystals of silver chalcogenides such as Ag_2Se and Ag_2Te with non-stochiometry as low as 1 part in 10^4. Here, the fluctuations in conductivity due to the inhomogeneities in the ion distributions and the application of high magnetic fields of a few T applied parallel to the current, is inferred to be at the origin of the NLMR [70,71]. Current jetting effects in topological semimetals are shown to depend on carrier mobility, on the mutual directions of the applied electric and magnetic fields and on the strength of the applied magnetic field. In the presence of a strong $\mu_0 H_\parallel$, the Weyl states in both WSM-I and WSM-II are quantized into Landau levels with the unique feature of the lowest Landau level (LLL) being chiral. The chiral charge density is given by $\rho^5 = (N_+ - N_-)/V$, where V is the sample volume and N_+ and N_- are the number of right handed and left handed chiral Weyl Fermions, respectively. The quantity ρ^5 is conserved until $E \parallel \mu_0 H_\parallel$. In terms of quantum field theory, $\nabla . J^5 + \partial_t \rho^5 = e\mathcal{C}$ where J^5 is the chiral current density and $\mathcal{C}$ is the anomaly term given by $\mathcal{C} = \left(e^2/4\pi^2\hbar^2\right)\mathbf{E}.\mu_0\mathbf{H}$. The conservation of ρ^5 is violated due to a non-zero $\mathcal{C}$ and the axial current is detected via negative $MR_\parallel$. Therefore, the chiral anomaly induced negative $MR_\parallel$ is a purely quantum effect involving the LLL and is observed on application of non-zero magnetic fields. On the other hand, in order to induce current jetting, the lower limit of the magnetic field $\mu_0 H_{cj}$ is given by the relation:

$$\mu_0 H_{cj} = \frac{\mathcal{C}}{\mu_{av}} \tag{5}$$

where μ_{av} is the average carrier mobility. The value of $\mathcal{C}$ is estimated to be ~(5–10) for topological semimetals [67]. From the measured $\mu_{av} \simeq 5000\,\text{cm}^2/\text{V.s}$ at $T = 5\,\text{K}$ of the samples studied in this work, the critical value of $\mu_0 H_{cj}$ is calculated to be ~10 T, which largely exceeds the maximum $\mu_0 H_\parallel = 7\,\text{T}$ used in this work. This is in contrast to the $\mu_0 H_{cj}$ reported for bulk crystals of WSM-I where the carrier mobilities were found to be as high as $\left(5 \times 10^6\right)\,\text{cm}^2/\text{V.s}$ at $T = 5\,\text{K}$, leading to $\mu_0 H_{cj} \leq 1\,\text{T}$ [64,67]. Additionally, the flakes studied here have a thickness of 45 nm, which is more than four orders of magnitude lower

than the one of bulk samples with dominant current jetting. Furthermore, the negative $MR_{\parallel}$ is observed only under the condition $\left[\mu_0 H_{\parallel} \parallel (E \parallel w) \right]$ for all the studied samples. No negative $MR_{\parallel}$ is recorded in S1, S2 and S3 for the condition $\left[\mu_0 H_{\parallel} \parallel (E \parallel l) \right]$, ruling out the geometric current jetting mechanism. The $MR_{\parallel}$ for S1 and S3 measured at $T = 5\,\mathrm{K}$ for both configurations, namely $\left[\mu_0 H_{\parallel} \parallel (E \parallel l) \right]$ and $\left[\mu_0 H_{\parallel} \parallel (E \parallel w) \right]$ are presented in Figure 8c. The obtained results indicate that the chiral anomaly can be observed only for a unique combination of the relative directions of E, $\mu_0 H_{\parallel}$ and w. In addition, as shown in Figure S6a,b in the Supplementary Materials, only a positive $MR_{\parallel}$ is measured for sample S4, where the flake is placed on the prefabricated contacts in such a way, that the w and l axes are misaligned w.r.t. the current and voltage leads with $(\mu_0 H \parallel E)$. If the current jetting would be the physical mechanism responsible for the observed negative $MR_{\parallel}$ for samples S1, S2 and S3, a similar result would have been observed for S4, where the flake thickness is identical to the one of the other three samples. Thus, it is concluded that the origin of the observed negative $MR_{\parallel}$ is due to the chiral anomaly in the WSM-II, WTe_2.

　　Moreover, two test samples are also studied, in which the metal contacts are fabricated on the exfoliated flakes by employing electron beam lithography (EBL). For both samples, the resistance is found to be $\sim 10^5\,\Omega$ and the samples display electronic properties befitting of a semiconductor. Such a change in the electronic behaviour in samples with contacts fabricated on flakes via EBL in comparison to the ones where the flakes are transferred onto the contacts, indicates that the exposure to chemicals and electron beams is detrimental for the semimetallic WTe_2 flakes considered in this work. Moreover, both Au and Pt are found to provide robust Ohmic contacts to thin exfoliated WTe_2 flakes.

3.4. Static Optical Reflectivity

　　Static reflectivity measurements as a function of T, $\mu_0 H_{\perp}$ and polarization of the incident light P_L have been performed on the exfoliated flakes. Optical reflectivity measured on WTe_2 in the far infra-red (IR) and in the mid IR energy range was reported to point at charge compensation from electron and hole pockets at the Fermi level [72–74]. Theoretical calculations based on *ab initio* density functional theory have predicted anisotropic optical reflectivity in WTe_2 for an energy range $0.5\,\mathrm{eV} \leq \hbar\omega \leq 3.5\,\mathrm{eV}$ as a function of the polarization [75]. Here, the experiments are carried out using a wide spectral range ultrafast pump-probe magneto-optical spectrometer at low-T/high-$\mu_0 H$[76]. In particular, the probe beam of this set-up is sent through an additional element for the generation of supercontinuum pulses to perform reflectivity measurements. The details of the experimental set-up are provided in the Supplementary Materials and the experimental arrangement is shown in Figure S1. The reflectivity spectra are recorded on a $\sim 45\,\mathrm{nm}$ thick exfoliated WTe_2 flake transferred onto a rigid SiO_2/p^{++}-Si substrate provided with markers to facilitate the identification of the flake under a microscope. The spectra are collected in the wavelength range between $450\,\mathrm{nm}$ and $700\,\mathrm{nm}$ at $T = 5\,\mathrm{K}$ and at $T = 300\,\mathrm{K}$ for $\mu_0 H_{\perp} = 0\,\mathrm{T}$ and for $\mu_0 H_{\perp} = 3\,\mathrm{T}$ and as a function of P_L, where the linear polarization of the supercontinuum pulses is rotated within the sample plane.

　　The spectrum of the generated supercontinuum pulses, measured after passing the beam through a color filter and a polarizer, is shown in Figure 9a for two perpendicular linear polarization directions corresponding to the electric field of light E_L, defined as: (i) $P_L = 120° \equiv \parallel$ and (ii) $P_L = 30° \equiv \perp$, such that E_L is respectively parallel and perpendicular to the long axis l of the measured WTe_2 flake, as shown in Figure 9b. The spectrum spans the spectral range between $450\,\mathrm{nm}$ to $700\,\mathrm{nm}$ and does not depend on the direction of the linear polarization. a detailed investigation (with longer acquisition time to increase the signal-to-noise ratio) for the two polarizations $P_L = \parallel$ and $P_L = \perp$ is performed and the results are presented in Figure S2 of the Supplementary Materials. The measured reflectivity spectra are normalized with respect to a reference spectrum recorded by diverting the laser beam before the sample and are reported in Figure 10a–d as a function of the polarization angle, of T, and of $\mu_0 H_{\perp}$. The spectra are shown as 2-

dimensional (2D) maps, where the intensity is encoded in color scale. As discussed in detail in the Supplementary Materials and shown in Figure S3, the reflectivity spectra recorded both at $T = 300\,\mathrm{K}$ and $T = 5\,\mathrm{K}$ show a dependence on P_{L}, that is more pronounced for $\mu_0 H_\perp = 3\,\mathrm{T}$ than for $\mu_0 H_\perp = 0\,\mathrm{T}$. This anisotropic behavior is in agreement with what observed in the magnetotransport studies. Moreover, a comparison of the spectra recorded at a fixed T reveals that the changes in the spectra upon application of $\mu_0 H_\perp = 3\,\mathrm{T}$ are more evident for $P_{\mathrm{L}} = \parallel$ then for $P_{\mathrm{L}} = \perp$. This behavior is elucidated quantitatively by evaluating the anisotropy A defined as:

$$A = \frac{R(3\,\mathrm{T}) - R(0\,\mathrm{T})}{R(0\,\mathrm{T})} \tag{6}$$

where $R(3\,\mathrm{T})$ and $R(0\,\mathrm{T})$ are the reflectivities measured for fixed light polarization and constant T in the presence and in the absence of magnetic field, respectively. As expected, the asymmetry is significantly pronounced in the data recorded for parallel light polarization. Thus, the magneto-optical reflectivity measurements complement the magnetotransport results and support the existence of anisotropic features in the electronic structure responsible for the observed out-of-plane electronic properties of the thin T_{d}-WTe$_2$ flakes.
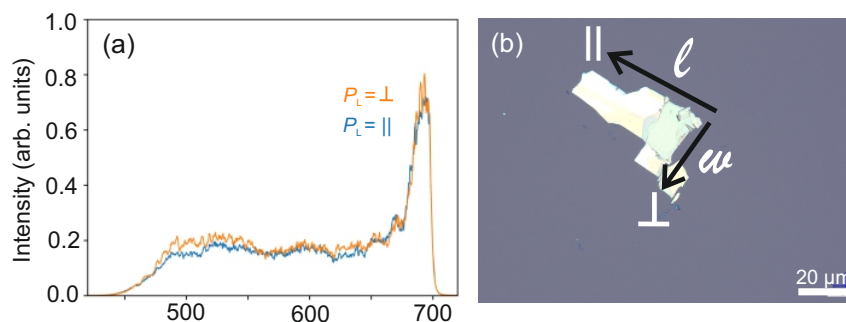

Figure 9. (**a**): Reference spectra of the supercontinuum pulses recorded for two crossed polarizations. The peak at $\sim$675 nm is associated with the seed pulse used for supercontinuum generation. (**b**): Optical microscopy image of the $\sim$45 nm T_{d}-WTe$_2$ sample. The directions of the linear polarization used in the experiments ($\parallel$ and $\perp$ to the flake long axis) are also indicated in the image.
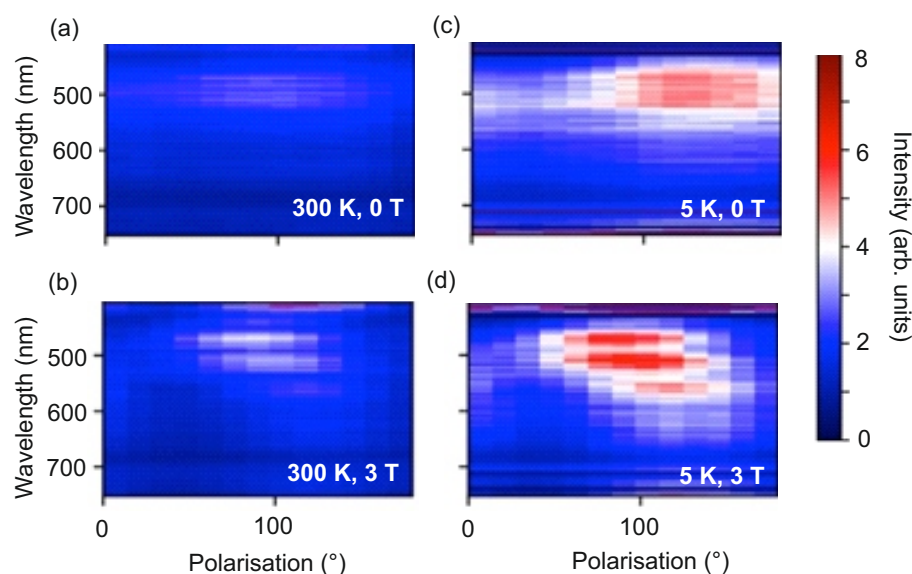

Figure 10. Reflectivity spectra for different T and $\mu_0 H_\perp$ as a function of the polarization for (**a**): $T = 300\,\mathrm{K}$, $\mu_0 H_\perp = 0\,\mathrm{T}$; (**b**): $T = 300\,\mathrm{K}$, $\mu_0 H_\perp = 3\,\mathrm{T}$; (**c**): $T = 50\,\mathrm{K}$, $\mu_0 H_\perp = 0\,\mathrm{T}$ and (**d**): $T = 5\,\mathrm{K}$, $\mu_0 H_\perp = 3\,\mathrm{T}$.

4. Conclusions

In summary, T_d-WTe$_2$ flakes of thickness $\sim$45 nm have been fabricated via mechanical exfoliation and transferred onto rigid SiO$_2$/p^{++}-Si substrates with prepatterned electrical contacts using a viscoelastic dry transfer technique. The flakes are found to be stable in air and no chemical degradation is observed over an aging period of seven days. The two exemplary samples reported–S1 and S2–are fabricated using 10 nm thick Pt metal pads as Ohmic contacts in a van der Pauw geometry and designed by photolithography. In S1, the relative orientation of the T_d-WTe$_2$ flake w.r.t. the four contact pads leads to an exact alignment of the directions of the applied electric field E and of the flake width w. In S2 the relative positions of the flake and the four Pt contacts result in a slight misalignment between E and w. Raman spectroscopic measurements carried out at room temperature reveal five Raman active modes, matching the theoretical predictions. The samples exhibit a large MR$_\perp$ as high as 1200% at $T = 5$ K and for a $\mu_0 H_\perp = 7$ T applied along the $c-$axis. A $\mu_0 H_\perp$-dependent turn-on T_{Trans} is observed, below which the samples undergo a MIT originating from the anisotropy of the Fermi surface. Both samples follow a Fermi liquid behavior for $T \leq 50$ K. The anisotropy of the Fermi surface – in combination with the presence of electron and hole pockets in the electronic band structure leading to charge compensation – is concluded to be at the origin of the large positive MR$_\perp$. The calculated $\mu_{\text{av}} \sim 5000$ cm^{2}V^{-1}s^{-1} at $T = 5$ K for S1 is a property of the Fermi liquid, while for $T \geq 50$ K the carrier mobility monotonically decreases due to the dominant electron-phonon coupling. The observed negative MR$_\parallel$ for $\left[\mu_0 H_\parallel \parallel (E \parallel w) \right]$ is a signature of chiral anomaly in T_d-WTe$_2$ and is found to be remarkably sensitive to the relative orientation of the $a-$ and $b-$axes w.r.t. the applied fields $\mu_0 H_\parallel$ and E. The observed chiral anomaly persists up to $T \sim 120$ K, a temperature at least four times higher than the one previously reported for WTe$_2$. A third sample S3 is also studied, which confirms the absence of current jetting, thereby allowing the conclusion that the quantum chiral anomaly is the origin of the observed negative MR$_\parallel$. The anisotropic behavior of the studied WSM-II system is confirmed by studying the optical reflectivity of the flakes as a function of T, $\mu_0 H$ and polarization of E_L in the visible range of the electromagnetic spectrum. It is also concluded, that the Weyl semimetallic properties of exfoliated thin flakes of WTe$_2$ are best observed when the flakes are transferred onto prefabricated metal Ohmic contacts, rather than when contacts are processed onto the flakes via EBL. The tunability of the large positive MR$_\perp$ and the chiral anomaly-driven negative MR$_\parallel$ as a function of the crystal axes and thickness, in combination with the chemical stability, pave the way for the application of 2D WSM-II WTe$_2$ in the future generation of chiral electronic devices like, e.g., chiral batteries, and as active elements for the detection of ultraweak magnetic fields [77].

Author Contributions: Conceptualization, R.A., S.A. and A.B.; methodology, R.A., S.A., B.F., M.T., S.B. and C.L.; formal analysis, R.A., S.A. and M.C.; investigation, R.A., S.A., M.C. and A.B.; writing—original draft preparation, R.A., A.B. and M.C.; writing—review and editing, R.A., A.B. and M.C.; vi-

Abbreviations

The following abbreviations are used in this manuscript:

MR	Magnetoresistance
WSM	Weyl semimetals
WQP	Weyl quasiparticles
ABJ	Adler–Bell–Jakiw
TMDC	Transition metal dichalcogenide
AFM	Atomic force microscopy
PDMS	Polydimethylsiloxane
LIA	Lock-in amplifier
ZFC	Zero field cooled
FC	Field cooled
MIT	Metal-to-insulator transition
NLMR	Negative longitudinal magnetoresistance
LLL	Lowest Landau level
EBL	Electron beam lithography
IR	Infra-red

References

1. Herring, C. Accidental Degeneracy in the Energy Bands of Crystals. *Phys. Rev.* **1937**, *52*, 365. [CrossRef]
2. Armitage, N.P.; Mele, E.J.; Vishwanath, A. Weyl and Dirac semimetals in three-dimensional solids. *Rev. Mod. Phys.* **2018**, *90*, 015001. [CrossRef]
3. Hasan, M.Z.; Xu, S.-Y.; Belopolski, I.; Huang, S.-M. Discovery of Weyl Fermion Semimetals and Topological Fermi Arc States. *Annu. Rev. Condens. Matter Phys.* **2017**, *8*, 289. [CrossRef]
4. Weyl, H. Elektron und Gravitation. I. *Z. Phys.* **1929**, *56*, 330. [CrossRef]
5. Xu, S.-Y.; Alidoust, N.; Belopolski, I.; Yuan, Z.; Bian, G.; Chang, T.-R.; Zheng, H.; Strocov, V.N.; Sanchez, D.S.; Chang, G.; et al. Discovery of a Weyl fermion state with Fermi arcs in niobium arsenide. *Nat. Phys.* **2015**, *11*, 748. [CrossRef]
6. Yang, L.X.; Liu, Z.K.; Sun, Y.; Peng, H.; Yang, H.F.; Zhang, T.; Zhou, B.; Zhang, Y.; Guo, Y.F.; Rahn, M.; et al. Weyl semimetal phase in the non-centrosymmetric compound TaAs. *Nat. Phys.* **2015**, *11*, 728. [CrossRef]
7. Lv, B.Q.; Xu, N.; Weng, H.M.; Ma, J.Z.; Richard, P.; Huang, X.C.; Zhao, L.X.; Chen, G.F.; Matt, C.E.; Bisti, F.; et al. Observation of Weyl nodes in TaAs. *Nat. Phys.* **2015**, *11*, 724. [CrossRef]
8. Wan, X.; Turner, A.M.; Vishwanath, A.; Savrasov, S.Y. Topological semimetal and Fermi-arc surface states in the electronic structure of pyrochlore iridates. *Phys. Rev. B* **2011**, *83*, 205101. [CrossRef]
9. Ilan, R.; Grushin, A.G.; Pikulin, D.I. Pseudo-electromagnetic fields in 3D topological semimetals. *Nat. Rev. Phys.* **2020**, *2*, 29. [CrossRef]
10. Dirac, P.A.M. The quantum theory of the electron. *Proc. R. Soc. Lond. A* **1928**, *117*, 610. [CrossRef]
11. Majorana, E. Teoria simmetrica dell'elettrone e del positrone. *II Nuovo Cimento* **1937**, *14*, 171. [CrossRef]
12. Yan, B.; Felser, C. Topological Materials: Weyl Semimetals. *Annu. Rev. Condens. Matter. Phys.* **2017**, *8*, 337. [CrossRef]
13. Nielsen, H.B.; Ninomiya, M. The Adler-Bell-Jackiw anomaly and Weyl fermions in a crystal. *Phys. Lett. B* **1983**, *130*, 389. [CrossRef]
14. Zhang, C.-L.; Xu, S.-Y.; Belopolski, I.; Yuan, Z.; Lin, Z.; Tong, B.; Bian, G.; Alidoust, N.; Lee, C.-C.; Huang, S.-M. Signatures of the Adler–Bell–Jackiw chiral anomaly in a Weyl fermion semimetal. *Nat. Commun.* **2016**, *7*, 10735. [CrossRef] [PubMed]

15. Lv, Y.-Y.; Li, X.; Zhang, B.-B.; Deng, W.Y.; Yao, S.-H.; Chen, Y.B.; Zhou, J.; Zhang, S.-T.; Lu, M.-H.; Zhang, L.; et al. Experimental Observation of Anisotropic Adler-Bell-Jackiw Anomaly in Type-II Weyl Semimetal $WTe_{1.98}$ Crystals at the Quasiclassical Regime. *Phys. Rev. Lett.* **2017**, *118*, 096603. [CrossRef] [PubMed]

16. Adler, S.L. Axial-Vector Vertex in Spinor Electrodynamics. *Phys. Rev.* **1969**, *177*, 2426. [CrossRef]

17. Bell, J.S.; Jackiw, R. A PCAC puzzle: $\pi_0 \rightarrow \gamma\gamma$ in the σ-model. *Il Nuovo Cimento A* **1969**, *60*, 47. [CrossRef]

18. Kang, K.; Li, T.; Sohn, E.; Shan, J.; Mak, K.F. Nonlinear anomalous Hall effect in few-layer WTe_2. *Nat. Mater.* **2019**, *18*, 324. [CrossRef]

19. Yesilyurt, C.; Tan, S.G.; Liang, G.; Jalil, M.B.A. Klein tunneling in Weyl semimetals under the influence of magnetic field. *Sci. Rep.* **2016**, *6*, 38862. [CrossRef] [PubMed]

20. Arjona, V.; Castro, E.V.; Vozmediano, M.A.H. Collapse of Landau levels in Weyl semimetals. *Phys. Rev. B* **2017**, *96*, 081110. [CrossRef]

21. Soluyanov, A.A.; Gresch, D.; Wang, Z.; Wu, Q.; Troyer, M.; Dai, X.; Bernevig, B.A. Type-II Weyl semimetals. *Nature* **2015**, *527*, 495. [CrossRef]

22. Tian, W.; Yu, W.; Liu, X.; Wang, Y.; Shi, J. A Review of the Characteristics, Synthesis, and Thermodynamics of Type-II Weyl Semimetal WTe_2. *Materials* **2018**, *11*, 1185. [CrossRef] [PubMed]

23. Bruno, F.Y.; Tamai, A.; Wu, Q.S.; Cucchi, I.; Barreteau, C.; de la Torre, A.; McKeown Walker, S.; Riccò, S.; Wang, Z.; Kim, T.K. Observation of large topologically trivial Fermi arcs in the candidate type-II Weyl semimetal WTe_2. *Phys. Rev. B* **2016**, *94*, 121112. [CrossRef]

24. Wu, Y.; Mou, D.; Jo, N.H.; Sun, K.; Huang, L.; Bud'ko, S.L.; Canfield, P.C.; Kaminski, A. Observation of Fermi arcs in the type-II Weyl semimetal candidate WTe_2. *Phys. Rev. B* **2016**, *94*, 121113. [CrossRef]

25. Das, P.K.; Di Sante, D.; Cilento, F.; Bigi, C.; Kopic, D.; Soranzio, D.; Sterzi, A.; Krieger, J.A.; Vobornik, I.; Fujii, J.; et al. Electronic properties of candidate type-II Weyl semimetal WTe_2. A review perspective. *Electron. Struct.* **2019**, *1*, 014003. [CrossRef]

26. Ong, N.P.; Liang, S. Experimental signatures of the chiral anomaly in Dirac–Weyl semimetals. *Nat. Rev. Phys.* **2021**, *3*, 394. [CrossRef]

27. Hosur, P.; Qi, X. Recent developments in transport phenomena in Weyl semimetals. *Comptes Rendus Phys.* **2013**, *14*, 857. [CrossRef]

28. Wang, Y.; Wang, L.; Liu, X.; Wu, H.; Wang, P.; Yan, D.; Cheng, B.; Shi, Y.; Watanabe, K.; Taniguchi, T.; et al. Direct Evidence for Charge Compensation-Induced Large Magnetoresistance in Thin WTe_2. *Nano Lett.* **2019**, *19*, 3969. [CrossRef]

29. Wang, Y.; Wang, K.; Reutt-Robey, J.; Paglione, J.; Fuhrer, M.S. Breakdown of compensation and persistence of nonsaturating magnetoresistance in gated WTe_2 thin flakes. *Phys. Rev. B* **2016**, *93*, 121108. [CrossRef]

30. Wang, Y.; Lee, P.A.; Silevitch, D.M.; Gomez, F.; Cooper, S.E.; Ren, Y.; Yan, J.-Q.; Mandrus, D.; Rosenbaum, T.F.; Feng, Y. Antisymmetric linear magnetoresistance and the planar Hall effect. *Nat. Commun.* **2020**, *11*, 216. [CrossRef]

31. Pan, X.-C.; Pan, Y.; Jiang, J.; Zuo, H.; Liu, H.; Chen, X.; Wei, Z.; Zhang, S.; Wang, Z.; Wan, X.; et al. Carrier balance and linear magnetoresistance in type-II Weyl semimetal WTe_2. *Front. Phys.* **2017**, *12*, 127203. [CrossRef]

32. Pan, X.-C.; Wang, X.; Song, F.; Wang, B. The study on quantum material WTe_2. *Adv. Phys. X* **2018**, *3*, 1468279. [CrossRef]

33. Liu, X.; Zhang, Z.; Cai, C.; Tian, S.; Kushwaha, S.; Lu, H.; Taniguchi, T.; Watanabe, K.; Cava, R.J.; Jia, S.; et al. Gate tunable magneto-resistance of ultra-thin WTe_2 devices. *2D Mater.* **2017**, *4*, 021018. [CrossRef]

34. Li, P.; Wen, Y.; He, X.; Zhang, Q.; Xia, C.; Yu, Z.-M.; Yang, S.A.; Zhu, Z.; Alshareef, H.N.; Zhang, X.-X. Evidence for topological type-II Weyl semimetal WTe_2. *Nat. Commun.* **2017**, *8*, 2150. [CrossRef]

35. Luo, X.; Fang, C.; Wan, C.; Cai, J.; Liu, Y.; Han, X.; Lu, Z.; Shi, W.; Xiong, R.; Zeng, Z. Magnetoresistance and Hall resistivity of semimetal WTe_2 ultrathin flakes. *Nanotechnology* **2017**, *28*, 145704. [CrossRef] [PubMed]

36. Deng, M.-X.; Qi, G.Y.; Ma, R.; Shen, R.; Wang, R.-Q.; Sheng, L.; Xing, D.Y. Quantum Oscillations of the Positive Longitudinal Magnetoconductivity: A Fingerprint for Identifying Weyl Semimetals. *Phys. Rev. Lett.* **2019**, *122*, 036601. [CrossRef] [PubMed]

37. Liang, D.D.; Wang, Y.J.; Zhen, W.L.; Yang, J.; Weng, S.R.; Yan, X.; Han, Y.Y.; Tong, W.; Zhu, W.K.; Pi, L.; et al. Origin of planar Hall effect in type-II Weyl semimetal $MoTe_2$. *AIP Adv.* **2019**, *9*, 055015. [CrossRef]

38. Deng, K.; Wan, G.; Deng, P.; Zhang, K.; Ding, S.; Wang, E.; Yan, M.; Huang, H.; Zhang, H.; Xu, Z. Experimental observation of topological Fermi arcs in type-II Weyl semimetal $MoTe_2$. *Nat. Phys.* **2016**, *12*, 1105. [CrossRef]

39. Xu, S.-Y.; Alidoust, N.; Chang, G.; Lu, H.; Singh, B.; Belopolski, I.; Sanchez, D.S.; Zhang, X.; Bian, G.; Zheng, H. Discovery of a Weyl fermion state with Fermi arcs in niobium arsenide. *Sci. Adv.* **2017**, *3*, e1603266. [CrossRef]

40. Ali, M.N.; Xiong, J.; Flynn, S.; Tao, J.; Gibson, Q.D.; Schoop, L.M.; Liang, T.; Haldolaarachchige, N.; Hirschberger, M.; Ong, N.P. Large, non-saturating magnetoresistance in WTe_2. *Nature* **2014**, *514*, 205. [CrossRef]

41. Ali, M.N.; Schoop, L.; Xiong, J.; Flynn, S.; Gibson, Q.; Hirschberger, M.; Ong, N.P.; Cava, R.J. Correlation of crystal quality and extreme magnetoresistance of WTe_2. *EPL* **2015**, *110*, 67002. [CrossRef]

42. Thoutam, L.R.; Wang, Y.L.; Xiao, Z.L.; Das, S.; Luican-Mayer, A.; Divan, R.; Crabtree, G.W.; Kwok, W.K. Temperature-Dependent Three-Dimensional Anisotropy of the Magnetoresistance in WTe_2. *Phys. Rev. Lett.* **2015**, *115*, 046602. [CrossRef] [PubMed]

43. Kononov, A.; Abulizi, G.; Qu, K.; Yan, J.; Mandrus, D.; Watanabe, K.; Taniguchi, T.; Schönenberger, C. One-Dimensional Edge Transport in Few-Layer WTe_2. *Nano Lett.* **2020**, *20*, 4228. [CrossRef] [PubMed]

44. Kononov, A.; Endres, M.; Abulizi, G.; Qu, K.; Yan, J.; Mandrus, D.G.; Watanabe, K.; Taniguchi, T.; Schönenberger, C. Flat band superconductivity in type-II Weyl-semimetal WTe_2 induced by a normal metal contact. *arXiv* **2020**, arXiv:2007.04752.

45. Huang, C.; Narayan, A.; Zhang, E.; Xie, X.; Ai, L.; Liu, S.; Yi, C.; Shi, Y.; Sanvito, S.; Xiu, F. Edge superconductivity in multilayer WTe$_2$ Josephson junction. *Natl. Sci. Rev.* **2020**, *7*, 1468. [CrossRef]

46. Shi, Y.; Kahn, J.; Niu, B.; Fei, Z.; Sun, B.; Cai, X.; Francisco, B.A.; Wu, D.; Shen, Z.-X.; Xu, X.; et al. Imaging quantum spin Hall edges in monolayer WTe$_2$. *Sci. Adv.* **2019**, *5*, eaat8799. [CrossRef]

47. Grundlinger, A. Optical and Electrical Investigation of Layered WSe$_2$ and MoS$_2$. Master's Thesis, Johannes Kepler University, Linz, Austria, 2018. Available online: https://epub.jku.at/obvulihs/content/titleinfo/2474933 (accessed on 23 March 2021).

48. Woods, J.M.; Shen, J.; Kumaravadivel, P.; Pang, Y.; Xie, Y.; Pan, G.A.; Li, M.; Altman, E.I.; Lu, L.; Cha, J.J. Suppression of Magnetoresistance in Thin WTe$_2$ Flakes by Surface Oxidation. *ACS Appl. Mater. Interfaces* **2017**, *9*, 23175. [CrossRef]

49. Wang, L.; Gutiérrez-Lezama, I.; Barreteau, C.; Ubrig, N.; Giannini, E.; Morpurgo, A.F. Tuning magnetotransport in a compensated semimetal at the atomic scale. *Nat. Commun.* **2015**, *6*, 8892. [CrossRef]

50. Augustin, J.; Eyert, V.; Böker, T.; Frentrup, W.; Dwelk, H.; Janowitz, C.; Manzke, R. Electronic band structure of the layered compound T$_d$–WTe$_2$. *Phys. Rev. B* **2000**, *62*, 10812. [CrossRef]

51. Jiang, Y.C.; Gao, J.; Wang, L. Raman fingerprint for semi-metal WTe$_2$ evolving from bulk to monolayer. *Sci. Rep.* **2016**, *6*, 19624. [CrossRef]

52. Zhang, E.; Chen, R.; Huang, C.; Yu, J.; Zhang, K.; Wang, W.; Liu, S.; Ling, J.; Wan, X.; Lu, H.-Z.; et al. Tunable Positive to Negative Magnetoresistance in Atomically Thin WTe$_2$. *Nano Lett.* **2017**, *17*, 878. [CrossRef] [PubMed]

53. Zhao, Y.; Liu, H.; Yan, J.; An, W.; Liu, J.; Zhang, X.; Wang, H.; Liu, Y.; Jiang, H.; Li, Q.; et al. Anisotropic magnetotransport and exotic longitudinal linear magnetoresistance in WTe$_2$ crystals. *Phys. Rev. B* **2015**, *92*, 041104. [CrossRef]

54. Abrikosov, A.A. *Fundamentals of the Theory of Metals*; Dover Publications: Amsterdam, The Netherlands, 2017.

55. Leahy, I.A.; Lin, Y.-P.; Siegfried, P.E.; Treglia, A.C.; Song, J.C.W.; Nandkishore, R.M.; Lee, M. Nonsaturating large magnetoresistance in semimetals. *Proc. Natl. Acad. Sci. USA* **2018**, *115*, 10570. [CrossRef] [PubMed]

56. Wang, K.; Graf, D.; Li, L.; Wang, L.; Petrovic, C. Anisotropic giant magnetoresistance in NbSb$_2$. *Sci. Rep.* **2014**, *4*, 7328. [CrossRef]

57. Takatsu, H.; Ishikawa, J.J.; Yonezawa, S.; Yoshino, H.; Shishidou, T.; Oguchi, T.; Murata, K.; Maeno, Y. Extremely Large Magnetoresistance in the Nonmagnetic Metal PdCoO$_2$. *Phys. Rev. Lett.* **2013**, *111*, 056601. [CrossRef] [PubMed]

58. Khveshchenko, D.V. Magnetic-Field-Induced Insulating Behavior in Highly Oriented Pyrolitic Graphite. *Phys. Rev. Lett.* **2001**, *87*, 206401. [CrossRef]

59. Pletikosić, I.; Ali, M.N.; Fedorov, A.V.; Cava, R.J.; Valla, T. Electronic Structure Basis for the Extraordinary Magnetoresistance in WTe$_2$. *Phys. Rev. Lett.* **2014**, *113*, 216601. [CrossRef]

60. Adhikari, R.; Volobuev, V.V.; Faina, B.; Springholz, G.; Bonanni, A. Ferromagnetic phase transition in topological crystalline insulator thin films: Interplay of anomalous Hall angle and magnetic anisotropy. *Phys. Rev. B* **2019**, *100*, 134422. [CrossRef]

61. Wang, Y.L.; Thoutam, L.R.; Xiao, Z.L.; Hu, J.; Das, S.; Mao, Z.Q.; Wei, J.; Divan, R.; Luican-Mayer, A.; Crabtree, G.W.; et al. Origin of the turn-on temperature behavior in WTe$_2$. *Phys. Rev. B* **2015**, *92*, 180402. [CrossRef]

62. Luo, Y.; Li, H.; Dai, Y.M.; Miao, H.; Shi, Y.G.; Ding, H.; Taylor, A.J.; Yarotski, D.A.; Prasankumar, R.P.; Thompson, J.D. Hall effect in the extremely large magnetoresistance semimetal WTe$_2$. *Appl. Phys. Lett.* **2015**, *107*, 182411. [CrossRef]

63. Wang, Y.; Liu, E.; Liu, H.; Pan, Y.; Zhang, L.; Zeng, J.; Fu, Y.; Wang, M.; Xu, K.; Huang, Z.; et al. Gate-tunable negative longitudinal magnetoresistance in the predicted type-II Weyl semimetal WTe$_2$. *Nat. Commun.* **2016**, *7*, 13142. [CrossRef]

64. Yang, J.; Zhen, W.L.; Liang, D.D.; Wang, Y.J.; Yan, X.; Weng, S.R.; Wang, J.R.; Tong, W.; Pi, L.; Zhu, W.K.; et al. Current jetting distorted planar Hall effect in a Weyl semimetal with ultrahigh mobility. *Phys. Rev. Mater.* **2019**, *3*, 014201. [CrossRef]

65. Reis, R.D.d.; Ajeesh, M.O.; Kumar, N.; Arnold, F.; Shekhar, C.; Naumann, M.; Schmidt, M.; Nicklas, M.; Hassinger, E. On the search for the chiral anomaly in Weyl semimetals: The negative longitudinal magnetoresistance. *New J. Phys.* **2016**, *18*. [CrossRef]

66. Schumann, T.; Goyal, M.; Kealhofer, D.A.; Stemmer, S. Negative magnetoresistance due to conductivity fluctuations in films of the topological semimetal Cd$_3$As$_2$. *Phys. Rev. B* **2017**, *95*, 241113. [CrossRef]

67. Liang, S.; Lin, J.; Kushwaha, S.; Xing, J.; Ni, N.; Cava, R.J.; Ong, N.P. Experimental Tests of the Chiral Anomaly Magnetoresistance in the Dirac-Weyl Semimetals Na$_3$Bi and GdPtBi. *Phys. Rev. X* **2018**, *8*, 031002. [CrossRef]

68. Li, Y.; Wang, Z.; Li, P.; Yang, X.; Shen, Z.; Sheng, F.; Li, X.; Lu, Y.; Zheng, Y.; Xu, Z.-A. Negative magnetoresistance in Weyl semimetals NbAs and NbP: Intrinsic chiral anomaly and extrinsic effects. *Front. Phys.* **2017**, *12*, 127205. [CrossRef]

69. Pippard, A.; Goldman, A.; McClintock, P.; Springford, M. *Magnetoresistance in Metals*; Cambridge Studies in Low Temperature Physics; Cambridge University Press: Cambridge, UK, 1989.

70. Hu, J.; Rosenbaum, T.F.; Betts, J.B. Current Jets, Disorder, and Linear Magnetoresistance in the Silver Chalcogenides. *Phys. Rev. Lett.* **2005**, *95*, 186603. [CrossRef] [PubMed]

71. Hu, J.; Parish, M.M.; Rosenbaum, T.F. Nonsaturating magnetoresistance of inhomogeneous conductors: Comparison of experiment and simulation. *Phys. Rev. B* **2007**, *75*, 214203. [CrossRef]

72. Homes, C.C.; Ali, M.N.; Cava, R.J. Optical properties of the perfectly compensated semimetal WTe$_2$. *Phys. Rev. B* **2015**, *92*, 161109. [CrossRef]

73. Kimura, S.-i.; Nakajima, Y.; Mita, Z.; Jha, R.; Higashinaka, R.; Matsuda, T.D.; Aoki, Y. Optical evidence of the type-II Weyl semimetals MoTe$_2$ and WTe$_2$. *Phys. Rev. B* **2019**, *99*, 195203. [CrossRef]

74. Santos-Cottin, D.; Martino, E.; Le Mardelé, F.; Witteveen, C.; von Rohr, F.O.; Homes, C.C.; Rukelj, Z.; Akrap, A. Low-energy excitations in type-II Weyl semimetal T$_d$–MoTe$_2$ evidenced through optical conductivity. *Phys. Rev. Mater.* **2020**, *4*, 021201. [CrossRef]

75. Rahman Rano, B.; Syed, I.M.; Naqib, S.H. Elastic, electronic, bonding, and optical properties of WTe2 Weyl semimetal: A comparative investigation with MoTe2 from first principles. *Results Phys.* **2020**, *19*, 103639. Available online: https://www.sciencedirect.com/science/article/pii/S2211379720320696 (accessed on 23 March 2021).

76. Mertens, F.; Terschanski, M.; Mönkebüscher, D.; Ponzoni, S.; Bossini, D.; Cinchetti, M. Wide spectral range ultrafast pump–probe magneto-optical spectrometer at low temperature, high-magnetic and electric fields. *Rev. Sci. Instrum.* **2020**, *91*, 113001. [CrossRef] [PubMed]

77. Kharzeev, D.E.; Yee, H.-U. Anomaly induced chiral magnetic current in a Weyl semimetal: Chiral electronics. *Phys. Rev. B* **2013**, *88*, 115119. [CrossRef]